PHYSICAL REVIEW E **83**, 030401(R) (2011)

Near-surface structure of a bicontinuous microemulsion with a transition region

M. Kerscher,[1] P. Busch,[2] S. Mattauch,[2] H. Frielinghaus,[2,*] D. Richter,[1,2] M. Belushkin,[3,4] and G. Gompper[3]
[1]*Institute for Solid State Research, Neutron Scattering, Forschungszentrum Jülich GmbH, D-52425 Jülich, Germany*
[2]*Jülich Centre of Neutron Science, Forschungszentrum Jülich GmbH, Lichtenbergstr. 1, D-85747 Garching, Germany*
[3]*Institute for Solid State Research, Theoretical Soft Matter and Biophysics, Forschungszentrum Jülich GmbH, D-52425 Jülich, Germany*
[4]*Institute of Theoretical Physics, Ecole Polytechnique Fédérale de Lausanne, CH-1015 Lausanne, Switzerland*
(Received 19 May 2010; revised manuscript received 2 December 2010; published 10 March 2011)

The lamellar ordering of bicontinuous microemulsions adjacent to a planar hydrophilic wall is investigated experimentally by grazing-incidence small-angle neutron scattering and theoretically by computer simulations. It is shown that precise depth information in neutron scattering can be obtained by tuning the scattering length density of the overall microemulsion. Neutron reflectometry completes the characterization. The nucleation of a lamellar phase at the wall is observed, and a perforated lamellar transition region is identified at the lamellar-microemulsion interface. The thickness of the lamellar region is about 400 Å, which corresponds to two bilayers.

DOI: 10.1103/PhysRevE.83.030401 PACS number(s): 82.70.Kj, 61.05.fj, 61.20.Gy, 64.60.Cn

The physics of condensed matter near surfaces can be understood only on the basis of a microscopic picture of the structure at the interface. Historically the most complete picture has emerged for interfaces of liquid metals or simple liquids [1]. These systems mostly tend toward *surface freezing*, also known as *surface ordering*. In a certain temperature range, the bulk material is liquid while the liquid/vapor interface has a higher degree of order, similar to a solid state. Contrarily, many soft-matter systems (i.e., complex fluids) tend toward *surface melting* [2]. On top of the well-ordered bulk material a thin layer with a lower degree of order is often found, even though Ref. [2], as a review, gives examples for surface ordering as well, for instance, polymeric micelles [3] or nanospheres [4]. Reflectometry and grazing-incidence small-angle scattering [4–12] became important methods for characterizing the surface near structure due to the selectivity by the small illuminated surface region. In studies of amphiphilic systems, monolayers [6] and several micelle layers [7,8] were found near the surface. Also, ordered lamellar structures were investigated with neutron [9] and x-ray [10] scattering techniques. First, results in resolving the surface region by grazing-incidence small-angle x-ray scattering and reflectometry experiments have been obtained with ferrofluids [11]. The grazing-incidence method is about to be transferred to dynamic studies [12]. Block copolymers and blends containing block copolymers [13] resemble microemulsions [14]. While block-copolymers melts and mixtures near walls have been studied [15–17], it is interesting to compare their behavior with that of amphiphilic microemulsions.

The surface of bicontinuous microemulsions was studied first by reflectometry [18,19]. The scattering-length density profile was obtained as a function of depth z in terms of a lateral average by a direct inversion method based on Parratt's recursion formalism [20], and a surface-induced layering was obtained. This density profile can be identified with an order-parameter profile that describes a high lamellar order near the surface decaying into the volume. This raises the question how the three-dimensional structure changes from the lamellar to the bicontinuous phase. Do undulations of the surfactant membrane increase until the lamellar order is destroyed? When does the lamellar phase lose its identity, and where does the bicontinuous structure emerge?

We have addressed the question of the structure of a bicontinuous microemulsion near a hydrophilic planar wall by computer simulations, neutron reflectometry (NR), and grazing-incidence small-angle neutron scattering (GISANS). The decay of the degree of order was confirmed by simulations and NR. Astonishingly, the intermediate structure was found to be perforated lamellae, so distinct well-separated holes are the reason for the decaying order parameter. Simulations and GISANS experiments give concrete depths of the different regions.

The samples consist of the nonionic surfactant $C_{10}E_4$ and equal amounts of oil and a H_2O/D_2O mixture. The H_2O/D_2O ratio was varied to obtain the desired scattering depth of the neutron wave. The neutron beam is reflected at the hydrophilic solid-liquid interface. All GISANS experiments were carried out at the small-angle neutron-scattering instrument KWS-2 [21], specular NR measurements at the reflectometer TREFF [22], and both at the reactor FRM II in Munich. Technical details about experiments can be found in the supporting material [23].

Monte Carlo calculations of the structure of microemulsions near hydrophilic surfaces have been performed in three-dimensional real space using a Ginzburg-Landau theory of ternary amphiphilic systems with a single scalar order parameter $\phi(\vec{r})$ that describes the local oil-water concentration difference [24]. The free-energy functional used is

$$\mathcal{F}[\phi] = \int d^3\vec{r}[(\Delta\phi)^2 + g(\phi)(\nabla\phi)^2 + f(\phi)]. \qquad (1)$$

The function g has the form $g = g_0 + g_2\phi^2$, and for f we took $f = (\phi+1)^2(\phi-1)^2(\phi^2 + f_0)$. The three minima of f correspond to pure oil, water, and surfactant domains. In order to be able to incorporate the planar surface, a surface term is added,

$$\mathcal{F}_s[\phi] = \int d^2\vec{r}[g_s(\phi)(\nabla\phi)^2 + \mu_s\phi + f_s(\phi)]. \qquad (2)$$

The wall is attractive for water, which is described by a chemical potential μ_s. Furthermore, the interaction of

*h.frielinghaus@fz-juelich.de

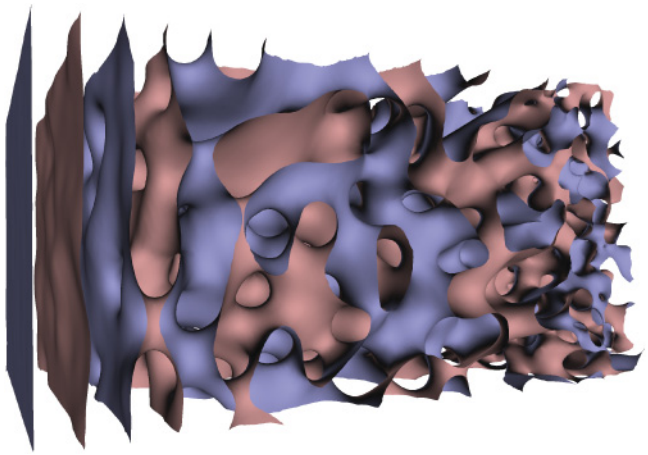

FIG. 1. (Color) Structure of the surfactant monolayer obtained in a computer simulation. Lamellar order is induced by the hydrophilic surface on the left (surface not shown). The order decays into the volume until the bicontinuous bulk structure is reached. A lamellar structure perforated by passages appears in the intermediate region.

molecules and their entropy will in general be different in the bulk and at the wall. This is accounted for with the local interaction term $f_s(\phi)$. Finally, a term related to the local chemical potential of the amphiphile at the wall can be included, $g(\phi)(\nabla\phi)^2$ [25]. Further details can be found in the supporting material [23]. An isosurface analysis of the order parameter reveals the structure of the surfactant monolayer at the interfaces between the oil-rich and water-rich regions (see Fig. 1). Order parameter profiles obtained in simulations have been used to calculate scattering length density distributions $\rho(\vec{r})$ from which theoretical predictions for neutron experiments are made. Reflectivity calculations are performed using Parratt's recursion formalism [20], and estimates of GISANS intensity distributions are obtained in the simple Born approximation taking the square of the Fourier transform and exponential dampening for the intensity.

The order parameter obtained in computer simulations [Fig. 2(a)] shows a perfect bilayer at the solid surface. The lamellar order decays with a typical length of about 300 Å (the simulation parameters have been adjusted to the bilayer thickness found by experiments). The bicontinuous bulk region is reached at around 500 Å away from the solid surface. Finally, the topology of the simulated structures is analyzed as follows. For each layer in the z direction, we calculate the number of perforations as the number of disconnected oil (water) regions in water- (oil-) rich layers. The density of passages is calculated as passage number density divided by the squared bilayer distance [Fig. 2(b)]. At small distnces from the wall, there are no perforations of the lamellae. The first peak at 100 Å is due to long-wavelength fluctuations of the lamellae. At distances above 500 Å the microemulsion is observed with a typical density of passages of ca. 0.04 in the simulation lattice. Between 200 and 500 Å we observe a perforated lamellar region, characterized by a large density of catenoid-like connections between the lamellae. The perforated lamellae region shows approximately double the amount of connections compared to the bicontinuous phase. This is due to the fact that in the perforated lamellae region

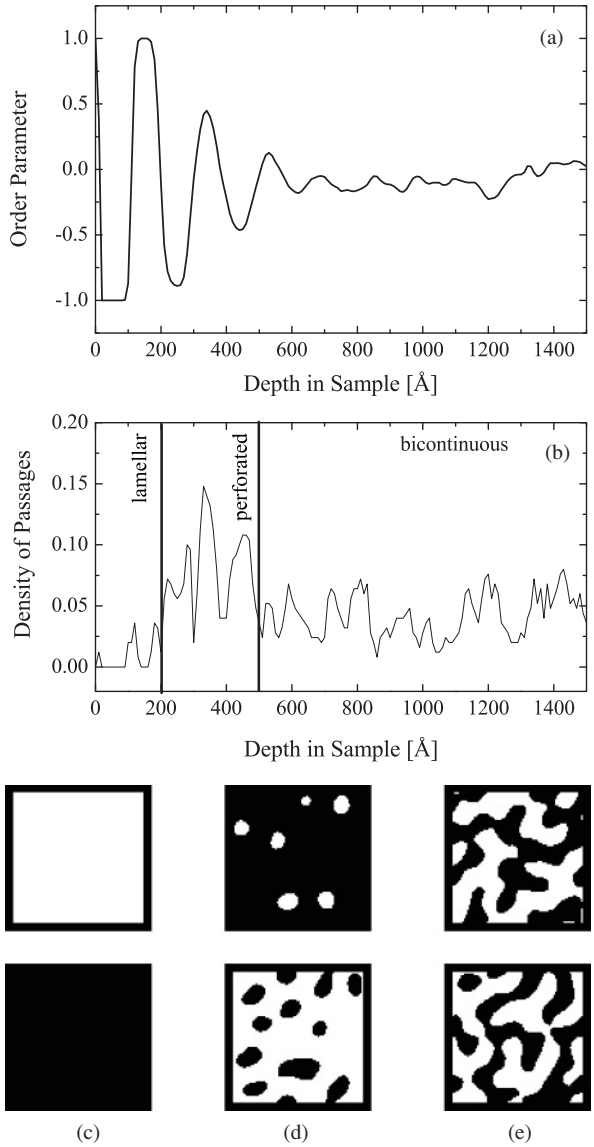

FIG. 2. (a) The order parameter indicating water (+1) and oil (−1) domains. A perfect double layer is found before the order decays into the volume. (b) Scaled passage density in the simulation box indicates that the transition region between 200 and 500 Å is a perforated lamellar structure. *Bottom:* Cuts parallel to the x-y plane through the simulation box. Black depicts oil, white water. (c) Cuts in the lamellar region (<100 Å), (d) in the preforated lamellar region (260 and 350 Å), and (e) in the bicontinuous bulk phase (ca. 1000 Å).

the passages are separately embedded inside the dominating component, whereas in the bicontinuous phase no dominating component exists, and, therefore, the domains appear more connected in the considered slices. This finding is also seen from the lateral cuts [Figs. 2(c)–2(d)]. Interestingly, the typical distances of the penetrating domains (especially for the layer at 350 Å) are very similar to the domain size observed in the bicontinuous region. Below we will argue that the simulated grazing-incidence scattering pattern does not strictly distinguish the scattering contributions from the perforated lamellae and the bicontinuous structure.

While GISANS is sensitive to both lateral and vertical correlations at the interface, specular NR probes the scattering

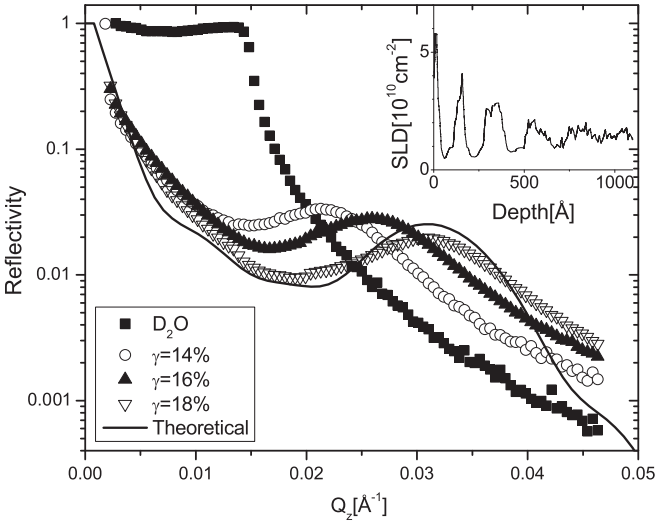

FIG. 3. Reflectivity curves of D_2O and samples with different surfactant concentrations. The continuous line bases on the Parratt algorithm for the simulated structure. The inset shows the real-space scattering length density profile for the $\gamma = 0.18$ sample based on the Parrat algorithm.

length density profile along the film normal. Figure 3 shows typical reflectivity curves for D_2O and different surfactant concentrations γ, with an overall scattering length density corresponding to a typical (GISANS) scattering depth $\Lambda_0 = (4\pi\,\Delta\rho)^{-1/2}$ of 800 Å. In the inset of Fig. 3 the real-space scattering length density profile of the sample with $\gamma = 18\%$ is shown. The profile was adjusted to the experimental reflectivity curve using the Parratt's recursion formalism [20]. As expected, alternating water and oil domains are found with decaying amplitudes into the bulk. The wavelength of the lamellar order gives rise to the peak of the reflectivity curve at $q_z \approx 0.025$ Å^{-1}. The real-space scattering length density resembles the order parameter of Fig. 2 to a high degree. The repeat distance of the lamellar phase is—in principle—dependent on the surfactant concentration however, in the range $\gamma = 15$–17% domain sizes of the bicontinuous and lamellar regions agree within experimental error.

In GISANS, measurements are performed at incident angles close to the critical angle $\alpha_c = \lambda\sqrt{\Delta\rho/\pi}$ of total internal reflection. In our case, typical values for the incident angles reach from 0.01° to 0.15°, which is below the critical angle of total reflection. In this regime, an evanescent (tunneling) wave propagates into the sample and gives rise to the scattering. The amplitude of this evanescent wave decays exponentially with a penetration length $\Lambda_{in} = [4\pi\,\Delta\rho(1 - \alpha_{in}^2/\alpha_c^2)]^{-1/2}$. Here α_{in} is the angle of the incident neutron beam, and $\Delta\rho$ is the difference of the scattering length densities of silicon and the overall microemulsion [17]. The scattering depth $\Lambda = (\Lambda_{in}^{-1} + \Lambda_{out}^{-1})^{-1}$ arises from the in- and outgoing waves ($\Lambda_{out} \approx \infty$ for $\alpha_{out} > \alpha_c$). Using D_2O/H_2O mixtures, we were able to reach scattering depths between 400 and 800 Å. Variation of both $\Delta\rho$ and α_{in} is especially important for neutron scattering. At low incident angles, the sample illumination is too low, while at angles close to the critical angle, the wavelength spread smears out the depth information of the scattering depth. While the incident wave is evanescent, the outgoing, scattered wave is at such high exit angles that refractive processes are negligible. Thus, the length scale of the evanescent wave is sensitive to the regions (lamellar or bicontinuous), while the scattering vector of the outgoing wave is comparable to the internal structure of the regions.

In GISANS, the preferred orientation of the lamellar phase gives rise to a peak in the scattering pattern (see Fig. 4). This pattern is described well by a Gaussian peak. The bicontinuous phase is locally isotropic, so the scattering from this phase leads to a ringlike structure. Both contributions can clearly be seen in the different graphs of Fig. 4. The scattering pattern of the bicontinuous phase can be modeled by the formula of Teubner and Strey [26]. While at high momentum transfers Q_z the patterns are not influenced by damping, close to $Q_z = 0$ additional damping becomes visible. There the outgoing wave becomes evanescent too. We do not observe any transmitted signals ($\alpha_{in} < \alpha_c$), and no Yoneda peak is observed ($\Delta\rho$ is small).

In the following, only the ratio I_{bic}/I_{lam} of the integrated intensities of the two phases is considered, which is difficult because the lamellar peak is superimposed on the bicontinuous ring. Therefore, we used a phenomenological fit function, which has four contributions: the lamellar peak, the

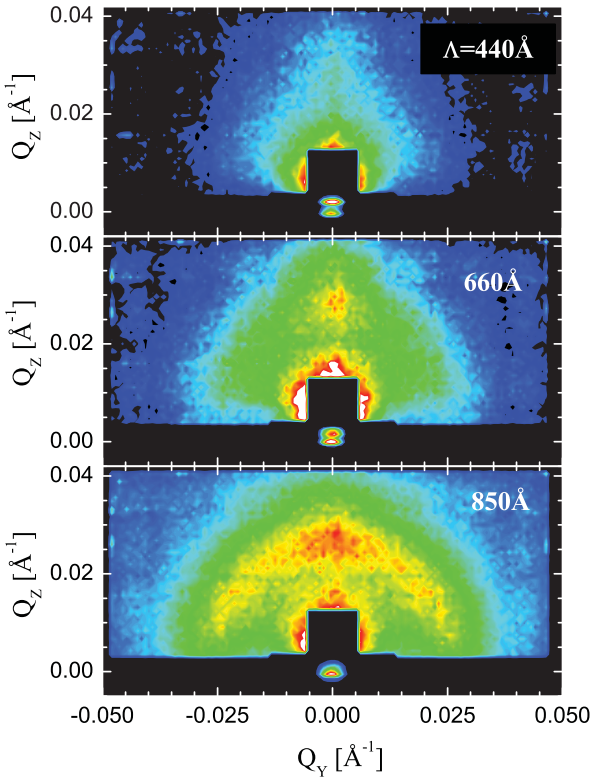

FIG. 4. (Color) Typical GISANS patterns at different scattering depths Λ: At $\Lambda = 440$ Å ($\alpha_{in} = 0.15°, \alpha_c = 0.29°$), a weak peak resulting from the lamellar phase is visible above the surface scattering. At $\Lambda = 660$ Å ($\alpha_{in} = 0.13°, \alpha_c = 0.21°$), the peak is clearly visible, and the ringlike scattering of the isotropic phase starts to appear. Finally, at $\Lambda = 850$ Å ($\alpha_{in} = 0.10°, \alpha_c = 0.16°$), the ring is clearly visible as well as the peak lying on top of it at the same Q_z value. The region containing the direct beam and the specular reflex was masked out for model fitting and is depicted by 2000 reduced intensity here. The top peak is the specular reflex, and the bottom one is the direct beam that passes the silicon block without reflection.

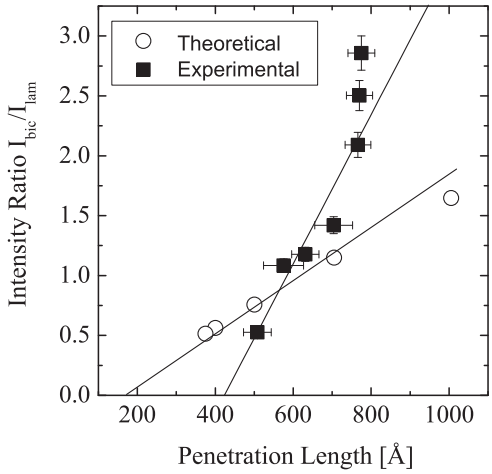

FIG. 5. Integral intensity ratio I_{bic}/I_{lam} of the scattering from the bicontinuous and the lamellar phase plotted against the scattering depth of the evanescent wave inside the lamellar phase. The open symbols are a result of the simulation (Fig. 1). Straight lines are guides for the eye.

bicontinuous ring, a contribution of the diffuse surface scattering, and a constant background (see supporting material [23]). The Q dependence of the four contributions was determined from measurements where their contribution was prominent. After that, only four amplitudes were fitted to the different scattering patterns. Figure 5 shows the integral intensity ratio plotted against the scattering depth Λ (similar to Ref. [27]). The experimental intensity ratio nearly vanishes for small scattering depths, which implies that the lamellar phase is the induced phase at the surface while the bicontinuous one is dominant in the bulk. Between 400 and 800 Å the relative intensity increases linearly, indicating more and more isotropic phase being illuminated. The intercept of the linear behavior is at ca. 400 Å. The simulated intensity ratio is also linear. The absolute values had to be scaled by a factor of three. An overestimated lamellar peak can be explained by the extremely sharp Bragg peak. For the integration we assumed the width of the peak to be one pixel. In this sense the lamellar intensity was overestimated. The extrapolated intercept of the simulations is ca. 200 Å, which indicates the depth of the perforated lamellae (Fig. 2). Thus, the measured length scale of the GISANS simulations is about half the experimental value. This finding agrees with the perforated lamellar structure at a depth between 200 and 500 Å scattering isotropically. Experimentally, the perforated lamellar structure extends from a depth of 400 Å, and the transition to the bicontinous phase is not resolved.

In summary, we found a good agreement between experiments and simulation. The simulated order parameter and the scattering length density from NR are laterally averaged and indicate the decaying order of the lamellae. The change from one-dimensional lamellar to three-dimensional bicontinuous structure is facilitated by a thin layer of perforated lamellae. In simulations the perforated lamellae contributed to the isotropic scattering. In experiments the isotropic structure emerges at 400 Å. The perforated lamellae might be observed experimentally more directly by other techniques in the future [28].

[1] O. Shpyrko, M. Fukuto, P. Pershan, B. Ocko, I. Kuzmenko, T. Gog, and M. Deutsch, Phys. Rev. B **69**, 245423 (2004).
[2] P. Lang, J. Phys. Condens. Matter **16**, R699 (2004).
[3] P. Lang, L. Willner, W. Pyckhout-Hintzen, and R. Krastev, Langmuir **19**, 7597 (2003).
[4] F. Cousin, J. Jestin, G. Chaboussant, S. Gautrot, A. Menelle, and F. Ott, Eur. Phys. J. **167**, 177 (2009).
[5] H. Dosch, B. W. Batterman, and D. C. Wack, Phys. Rev. Lett. **56**, 1144 (1986).
[6] R. Steitz, P. Müller-Buschbaum, S. Schemmel, R. Cubitt, and G. Findenegg, Europhys. Lett. **67**, 962 (2004).
[7] M. Wolff, U. Scholz, R. Hock, A. Magerl, V. Leiner, and H. Zabel, Phys. Rev. Lett. **92**, 255501 (2004).
[8] W. Hamilton, L. Porcar, and L. Magid, Physica B **357**, 88 (2005).
[9] G. Salamat, R. de Vries, and E. Kaler, Langmuir **16**, 102 (2000).
[10] G. Brotons, L. Belloni, T. Zemb, and T. Salditt, Europhys. Lett. **75**, 992 (2006).
[11] A. Vorobiev, G. Gordeev, O. Konovalov, and D. Orlova, Phys. Rev. E **79**, 031403 (2009).
[12] B. Cichocki, E. Wajnryb, J. Blawzdziewicz, J. K. G. Dhont, and P. Lang, J. Chem. Phys. **132**, 074704 (2010).
[13] N. R. Washburn, T. P. Lodge, and F. S. Bates, J. Phys. Chem. **104**, 6987 (2000).
[14] W. M. Gelbart, A. Ben-Shaul, and D. Roux, *Micelles, Membranes, Microemulsions, and Monolayers* (Springer, New York, 1994).
[15] M. W. Matsen and M. Schick, Macromolecules **26**, 3878 (1993).
[16] R. R. Netz, D. Andelman, and M. Schick, Phys. Rev. Lett. **79**, 1058 (1997).
[17] P. Müller-Buschbaum, L. Schulz, E. Metwalli, J. F. Moulin, and R. Cubitt, Langmuir **24**, 7639 (2008).
[18] X.-L. Zhou, L.-T. Lee, S.-H. Chen, and R. Strey, Phys. Rev. A **46**, 6479 (1992).
[19] D. D. Lee, S. H. Chen, C. F. Majkrzak, and S. K. Satija, Phys. Rev. E **52**, R29 (1995).
[20] L. G. Parratt, Phys. Rev. **95**, 359 (1954).
[21] A. Radulescu and A. Ioffe, Nucl. Instrum. Meth. A **586**, 55 (2008).
[22] U. Rücker, B. Alefeld, E. Kentzinger, and T. Brückel, Physica B **283**, 422 (2000).
[23] See supplemental material at [http://link.aps.org/supplemental/10.1103/PhysRevE.83.030401] for experimental and simulation details.
[24] G. Gompper and M. Schick, Phys. Rev. Lett. **65**, 1116 (1990).
[25] G. Gompper and S. Zschocke, Phys. Rev. A **46**, 4836 (1992).
[26] M. Teubner and R. Strey, J. Chem. Phys. **87**, 3195 (1987).
[27] E. Filippidi, V. Michailidou, B. Loppinet, J. Rühe, and G. Fytas, Langmuir **23**, 5139 (2007).
[28] Y. Nishikawa, H. Jinnai, T. Koga, T. Hashimoto, and S. T. Hyde, Langmuir **14**, 1242 (1998).